Self-Rolled-Up Ultrathin Single-Crystalline Silicon Nanomembranes for On-Chip Tubular Polarization Photodetectors

*Binmin Wu, Ziyu Zhang, Zhi Zheng, Tianjun Cai, Chunyu You, Chang Liu, Xing Li, Yang Wang, Jinlong Wang, Hongbin Li, Enming Song, Jizhai Cui, Gaoshan Huang, and Yongfeng Mei**

Freestanding single-crystalline nanomembranes and their assembly have broad application potential in photodetectors for integrated chips. However, the release and self-assembly process of single-crystalline semiconductor nanomembranes still remains a great challenge in on-chip processing and functional integration, and photodetectors based on nanomembrane always suffer from limited absorption of nanoscale thickness. Here, a non-destructive releasing and rolling process is employed to prepare tubular photodetectors based on freestanding single-crystalline Si nanomembranes. Spontaneous release and self-assembly are achieved by residual strain introduced by lattice mismatch at the epitaxial interface of Si and Ge, and the intrinsic stress and strain distributions in self-rolled-up Si nanomembranes are analyzed experimentally and computationally. The advantages of light trapping and wide-angle optical coupling are realized by tubular geometry. This Si microtube device achieves reliable Ohmic contact and exhibits a photoresponsivity of over 330 mA W^{-1}, a response time of 370 µs, and a light incident detection angle range of over 120°. Furthermore, the microtubular structure shows a distinct polarization angle-dependent light absorption, with a dichroic ratio of 1.24 achieved at 940 nm. The proposed Si-based microtubes provide new possibilities for the construction of multifunctional chips for integrated circuit ecosystems in the More than Moore era.

1. Introduction

Freestanding semiconductor nanomembranes with high crystallinity exhibit excellent photonic and optoelectronic properties.[1–3] Tuning the thickness of freestanding nanomembranes usually only affects their mechanical properties,[4,5] such as Young's modulus and stiffness, without affecting its bandgap. This characteristic is advantageous for the manufacture of flexible devices with 3D geometry.[6,7] 3D self-assembled freestanding nanomembranes offer a wider range of optical functions and mechanical structural designs than 2D planar materials.[8–10] Typically, the fabrication process of freestanding 3D single-crystalline nanomembranes relies on heterogeneous epitaxial techniques with lattice interfaces and artificial termination first,[11–14] which is often considered as lattice matching. During epitaxial processes, residual strain will be inevitably introduced into epitaxial single-crystalline nanomembranes via lattice mismatch, which often results in a short lifetime and poor uniformity of planar devices.[15–17] Nevertheless, proper use of residual strain can also yield additional benefits. For example, in order to support the development of Moore's Law, internal stress and strain are introduced into Si and Ge to adjust the energy band structure and improve carrier mobility.[18–20] The epitaxial nanomembranes are then separated from the substrate by layer separation techniques (e.g., chemical lift-off, 2D-assisted lift-off, mechanical spalling).[1,4,21,22] The released

B. Wu, Z. Zhang, Z. Zheng, T. Cai, C. You, C. Liu, X. Li, Y. Wang, J. Wang, H. Li, J. Cui, G. Huang, Y. Mei
Department of Materials Science & State Key Laboratory of ASIC and Systems
Fudan University
Shanghai 200438, P. R. China
E-mail: yfm@fudan.edu.cn

E. Song, J. Cui, G. Huang, Y. Mei
Yiwu Research Institute of Fudan University
Yiwu 322000, P. R. China

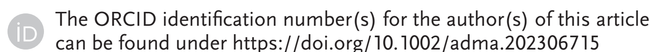
The ORCID identification number(s) for the author(s) of this article can be found under https://doi.org/10.1002/adma.202306715

DOI: 10.1002/adma.202306715

E. Song, J. Cui, G. Huang, Y. Mei
International Institute of Intelligent Nanorobots and Nanosystems
Fudan University
Shanghai 200438, P. R. China

E. Song, Y. Mei
Shanghai Frontiers Science Research Base of Intelligent Optoelectronics and Perception
Institute of Optoelectronics
Fudan University
Shanghai 200438, P. R. China

 © 2023 Wiley-VCH GmbH

single-crystalline nanomembranes can then be assembled to fabricate 3D electronic devices with targeted functions such as high-performance lasers,[23] memories,[11] and photodetectors.[1]

Rolled-up nanomembranes,[6,8,24] as a fast-evolving technology, can be combined with existing chip manufacturing methods to convert specified 2D precursor structures into micro/nano tubular devices with 3D geometries,[7,10] which can offer a promising chip integration platform by forming 3D volumetric devices with a more compact aerial footprint. Therefore, self-rolled-up technology can be used as a new integration technology to roll up centimeter-scale nanomembranes into micro-scale microtubes, which has been effectively utilized to fabricate devices such as field-effect transistors,[25] heterostructure,[9] and memory.[26] In addition, a rolled-up nanomembrane can introduce stress to adjust the band gap and carrier transport of the semiconductor,[27,28] and a rolled-up nanomembrane microtube can also act as a whispering-gallery optical microcavity or optical trap.[29,1] Hence, the integration of rolled-up nanomembrane technology with Si, the foremost semiconductor material in today's integrated circuit industry, offers significant advantages and is a promising approach to electronic and optoelectronic technological advancement. Currently, epitaxy Si nanomembranes on Si, Ge, and $Si_{1-x}Ge_x$ substrates are highly advanced technologies that have been extensively utilized in state-of-the-art integrated circuit manufacturing.[30–32] Typically, the epitaxial interface between Si and Ge can induce ≈4.18% interfacial strain.[33–35] When the epitaxial single-crystalline Si nanomembrane on Ge or $Si_{1-x}Ge_x$ sacrificial layer is released, residual stress at the epitaxial interface can spontaneously drive the formation of 3D structures, including tubular and wrinkled structures,[7,36,37] which is a solid foundation for the preparation of 3D Si nanomembranes electronic and optoelectronic devices.

In this article, we used etchant to selectively etch the Ge sacrificial layer and to release single-crystalline Si nanomembranes. The released Si nanomembranes rolled up into microtubes. The high-angle annular dark-field scanning transmission electron microscopy (HAADF-STEM) image shows that the self-rolled-up Si nanomembranes preserve an excellent single-crystalline structure. Through the analysis of microtubes with varying thicknesses, the relationship between the diameter of microtubes and the thickness of Si nanomembranes is obtained, and the strain distribution of Si nanomembranes after self-rolled-up is calculated. Based on the analysis, the electrical transport mechanism and photoresponse in visible/near-infrared spectroscope (VIS-NIRs) of Si microtubes are studied. Remarkably, the Si microtubular photodetector not only demonstrates wide-angle incident light detection but also suggests promising potential for future polarized light detection.

2. Results and Discussion

2.1. Fabrication and Characterization of Single-Crystalline Si Microtubes

Epitaxy of Si nanomembrane on Ge is a well-developed technology in the field of epitaxial semiconductor materials. **Figure 1**a shows a cross-sectional HAADF-STEM image near the Si/Ge epitaxial interface. Single-crystalline Si nanomembranes are epitaxially grown on Ge (001) by molecular beam epitaxy (MBE). Ge serves as a sacrificial layer that can be dissolved in the hydrogen peroxide (H_2O_2) solution. The right side of Figure 1a shows the fast Fourier transform (FFT) pattern of the epitaxial Si/Ge interface, revealing excellent single-crystalline quality and hetero-epitaxial interface. The two separate diffraction spots located at both (004) and $(0\bar{4}0)$ corresponds to the interplanar spacing of Si and Ge, respectively. The SEAD patterns of Si and Ge without epitaxial interfaces are shown in Figure S1, Supporting Information. The red spots represent Si with a (004) and $(0\bar{4}0)$ interplanar spacing of ≈0.143 nm, and the orange spots correspond to Ge with a (004) and $(0\bar{4}0)$ interplanar spacing of ≈0.150 nm. The mismatches of the (220) crystal plane of Si and Ge at the epitaxial interface are analyzed in Figure S2a, Supporting Information. Lattice mismatch of Si and Ge results in tensile strain on the single-crystalline Si nanomembrane at the epitaxial interface, and correspondingly, introduces compressive strain on Ge at the epitaxial interface. We calculated strain maps of ϵ_{xx}, which range from −5% to +5% by using geometrical phase analysis at atomic scale,[11,12] as shown in Figure 1b and Figure S2b, Supporting Information.

We fabricated the Si/Ge bilayer into an array of squares with a fixed end by photolithography and reaction ion etching, as shown in Figure 1c. The Si layer was immersed in the H_2O_2 solution at 70 °C for several minutes until the Si nanomembranes were separated from the substrate and spontaneously rolled up (Figure S3, Supporting Information). Figure 1d shows a self-rolled-up microtube array of Si nanomembrane with a thickness of 30 nm. Similarly, self-rolled-up microtubes of Si nanomembranes with a thickness of 20 nm are shown in Figure S4, Supporting Information. The self-rolled-up behaviors are due to the internal strain caused by the different lattice constants between Si and Ge. During the epitaxial process, tensile and compressive strains were introduced by lattice mismatch between different layers. Specifically, the lattice constants of Si and Ge, both of which also have diamond structures, are 0.543 and 0.566 nm,[38,39] respectively. The tensile strain in epitaxial Si nanomembranes is confirmed by wavelength-dependent Raman spectroscopy, as shown in Figure S5, Supporting Information. During the epitaxial Si nanomembrane release process, the lower surface experiences a larger tensile strain compared to the upper surface, leading to a downward self-rolled-up of the released Si nanomembrane. In order to strengthen the sample, an 80-nm-thick aluminum oxide (Al_2O_3) layer was coated on the self-rolled-up Si microtubes via atomic layer deposition (ALD) to stabilize the tubular structure and protect the crystal structure from destruction during focused ion beam (FIB) cutting and sample preparation. By removing an arched sample from the Si microtube wall with FIB, the tightly bonded self-rolled-up Si nanomembranes between the Al_2O_3 layers were observed, as shown in Figure 1e and Figure S6, Supporting Information. The Si layer below Al_2O_3 is formed by ion bombardment of Si and sputtering on the inner wall of the microtube during the FIB sampling process. Figure 1f shows an enlarged TEM image of a small segment of the Si microtube wall. The inner side of each tube wall is the epitaxial interface of Si and Ge, which is significantly flatter than the exposed surface on the outside. Impurity particles between layers are likely to be introduced after wet etching and critical point drying. Figure 1g shows an atomic scale HAADF-STEM image of the Si microtube, demonstrating that the self-rolled-up Si nanomembrane

© 2023 Wiley-VCH GmbH

15214095, 2023, 52, Downloaded from https://advanced.onlinelibrary.wiley.com/doi/10.1002/adma.202306715 by Fudan University, Wiley Online Library on [29/01/2026]. See the Terms and Conditions (https://onlinelibrary.wiley.com/terms-and-conditions) on Wiley Online Library for rules of use; OA articles are governed by the applicable Creative Commons License

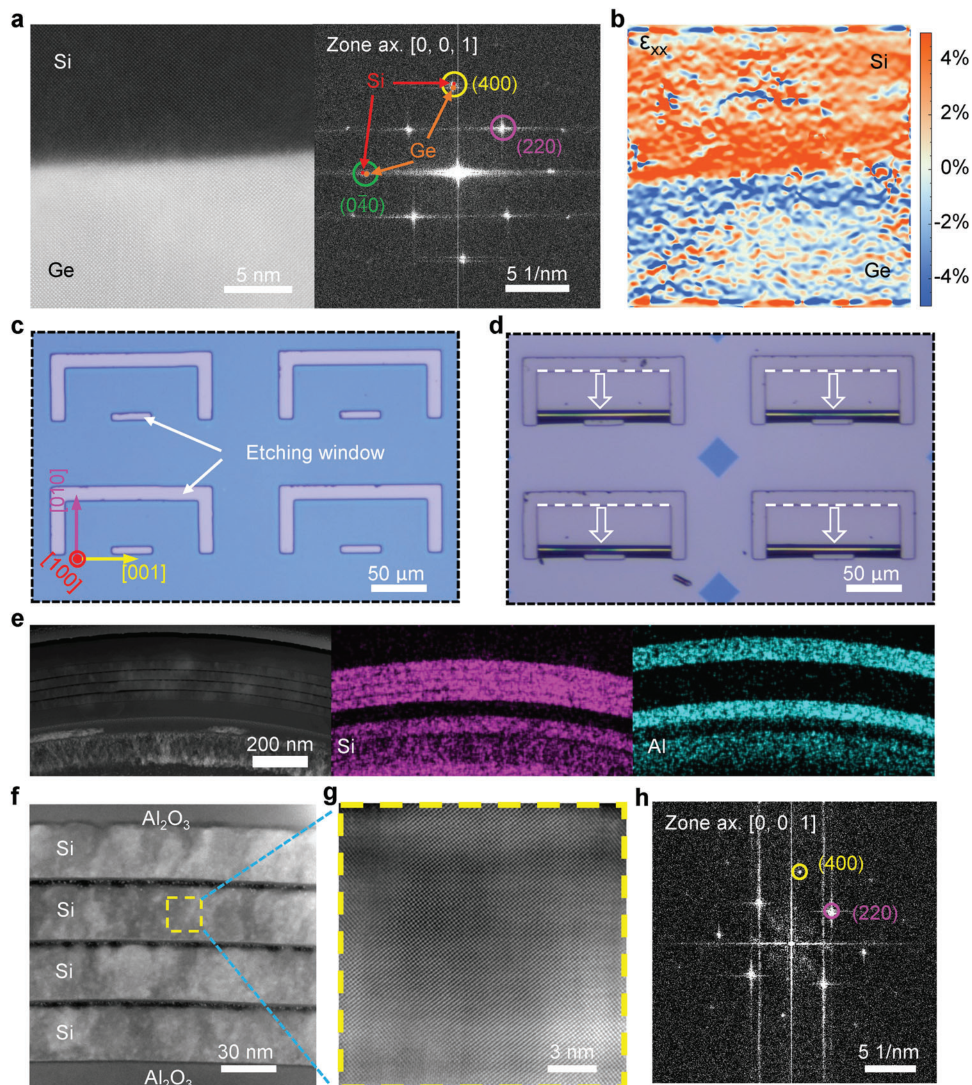

Figure 1. Fabrication of self-rolled-up single crystalline Si microtube. a) Cross-sectional HAADF-STEM image of the interface of epitaxial Si grown on Ge (left panel), viewed along [001] zone axis and corresponding FFT pattern (right panel). b) Geometric phase analysis image of in-plane strain distribution near the Si/Ge interface corresponding to panel (a). c) Optical image of the flat and pre-patterned Si nanomembranes with etching windows. d) Optical image of self-rolled-up Si microtubes. e) Low-magnification cross-sectional TEM image of the self-rolled-up Si microtube wall and the corresponding chemical element distribution. f) A zoomed-in STEM image of the self-rolled-up Si multilayer. g) Atomic-resolution HAADF-STEM image and the corresponding FFT pattern of self-rolled-up Si nanomembrane (h).

maintains a complete single-crystalline structure after release. The corresponding FFT pattern is shown in Figure 1h. In addition, our self-rolled-up Si nanomembrane microtubes are tightly rolled and stuck layer by layer, with a gap of about 3–4 nm. Moreover, the gap in the most compact region is as short as 1 nm, and a clear atomic structure can also be observed (Figure S7, Supporting Information). Typically, the rolled-up direction of the isotropic nanomembrane is mainly modulated by the pre-strain and the predetermined pattern.[40,41] However, the self-rolled-up direction of epitaxial nanomembranes is limited by the crystal orientation.[6,42] By polarization Raman characterization,[43,44] we found that the angle between the rolling direction of microtubes and the lattice direction is about 9.90° (Figures S8 and S9, Supporting Information), showing excellent geometrical control.

2.2. Strain Analysis of Self-Rolled-Up Si Nanomembranes

We prepared self-rolled-up microtubes based on epitaxial Si nanomembranes with thicknesses of 6, 10, 20, and 30 nm, and the corresponding XRD characterizations are shown in Figure S10, Supporting Information. **Figure 2**a shows a self-rolled-up microtube, and the Si microtube has no visible collapse and no significant gaps in the tube walls. More high-resolution scanning electron microscopy (SEM) images are used to count the radius distribution of Si microtubes (Figure S11, Supporting Information). For 6, 10, 20, and 30 nm Si nanomembranes, the diameters of the microtubes are ≈0.7, 1.1, 3.9, and 8.3 µm, respectively, as shown in Figure 2b. In order to analyze the relationship between the geometric characteristics and strain

 © 2023 Wiley-VCH GmbH

15214095, 2023, 52, Downloaded from https://advanced.onlinelibrary.wiley.com/doi/10.1002/adma.202306715 by Fudan University, Wiley Online Library on [29/01/2026]. See the Terms and Conditions (https://onlinelibrary.wiley.com/terms-and-conditions) on Wiley Online Library for rules of use; OA articles are governed by the applicable Creative Commons License

15214095, 2023, 52, Downloaded from https://advanced.onlinelibrary.wiley.com/doi/10.1002/adma.202306715 by Fudan University, Wiley Online Library on [29/01/2026]. See the Terms and Conditions (https://onlinelibrary.wiley.com/terms-and-conditions) on Wiley Online Library for rules of use; OA articles are governed by the applicable Creative Commons License

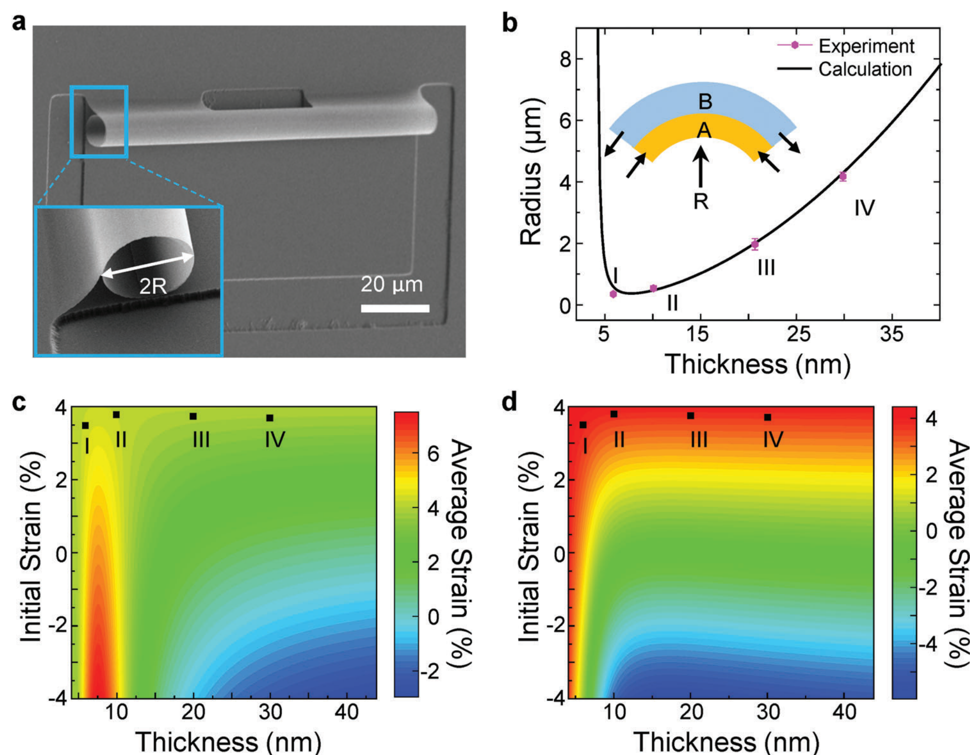

Figure 2. Thickness-dependent radius and corresponding strain distribution of Si nanomembrane microtube. a) SEM image of a self-rolled-up Si microtube. Inset: enlarged side view of the microtube. b) Calculation of the relationship between the radius of the Si microtube and the nanomembrane thickness. The experimental results of tuning the Si nanomembrane thickness are plotted on the curve (I, II, III, and IV). The inset shows the formation mechanism for the strain-induced self-rolled-up of the epitaxial Si nanomembrane. Mappings of the bending-induced c) compressive and d) tensile strains related to the thickness of the Si layer with different initial strains. Spots I, II, III, and IV are the same samples as in panel (b).

distribution of Si self-rolled-up nanomembranes, the thickness and initial strain must be considered. As the Si nanomembrane is a monolayer consisting of a single material, applying Nikishkov's multilayer nanomembrane rolled-up theoretical model formula may encounter insurmountable challenges.[45] Here, an ideal strain model is proposed to solve the strain distribution problem in single-crystalline epitaxial monolayer nanomembranes. Si/Ge lattice mismatch is significantly reduced from the interface in the distance of several molecular layers. Thus, the single-layer epitaxial nanomembrane can be divided into two ideal layers, wherein layer A is near the epitaxial interface and has a higher strain and the other layer B is away from the epitaxial interface and has a lower strain. Then we define the following parameters: the thickness of the Si nanomembrane and two ideal layers t_{Si}, t_A, t_B, initial strain of two ideal layers ϵ_A, ϵ_B, in which $t_{Si} = t_A + t_B$, $\Delta\epsilon = \epsilon_A - \epsilon_B$. For pre-strained nanomembranes, the parametric solution of the nanomembrane radius after rolling is obtained by force and moment equilibrium equations[27,45]

$$R\left(t_A, \Delta\epsilon\right) = \frac{t_A^4 + (t_{Si} - t_A)^4 + 2t_A(t_{Si} - t_A)\left(2t_A^2 + 2(t_{Si} - t_A)^2 + 3t_A(t_{Si} - t_A)\right)}{6t_A(t_{Si} - t_A)t_{Si}\Delta\epsilon} \quad (1)$$

Based on this equation, the corresponding results of t_A and $\Delta\epsilon$ are obtained by traversing the parameters on ϵ_A, ϵ_B, and t_A in different total thicknesses of Si nanomembrane (t_{Si} = 6/10/20/30 nm), and collected from the intersection of the sets of solutions satisfying the corresponding diameters of self-rolled-up Si microtubes. As shown in Figure 2b, the calculated results of the relationship between the radius and thickness of Si nanomembrane are consistent with the experimental results. It is worth noting that the deposition of functional thin films (such as metallic electrodes) onto the epitaxial Si nanomembrane will alter the strain distribution within the epitaxial Si nanomembrane, ultimately resulting in a corresponding adjustment in the diameter of the Si microtube. The average strain in ideal layers A and B are exhibited in Figures 2c,d, respectively. Initial strains of layer B in Si nanomembranes of different thicknesses were 3.49% (I), 3.79% (II), 3.75% (III), and 3.71% (IV), respectively, as shown in Figure 2d. According to the corresponding experimental data points and minimum elastic energy theory, the tensile strains of both layer A and layer B exhibit varying degrees of decrease after release due to the requirements for force balance and moment balance of the two layers. This proposed ideal layer model is not only suitable for Si nanomembranes but also for geometric prediction and strain analysis of various epitaxial single-crystalline nanomembranes.

2.3. Electrical Properties of Si Microtubes

In addition to doping impurities, the electrical properties of ultrathin Si nanomembranes are distinctly affected by their surface/interface[5,46] such as lattice defects, surface dangling bonds, and organic residues. Generally, the surface of

© 2023 Wiley-VCH GmbH

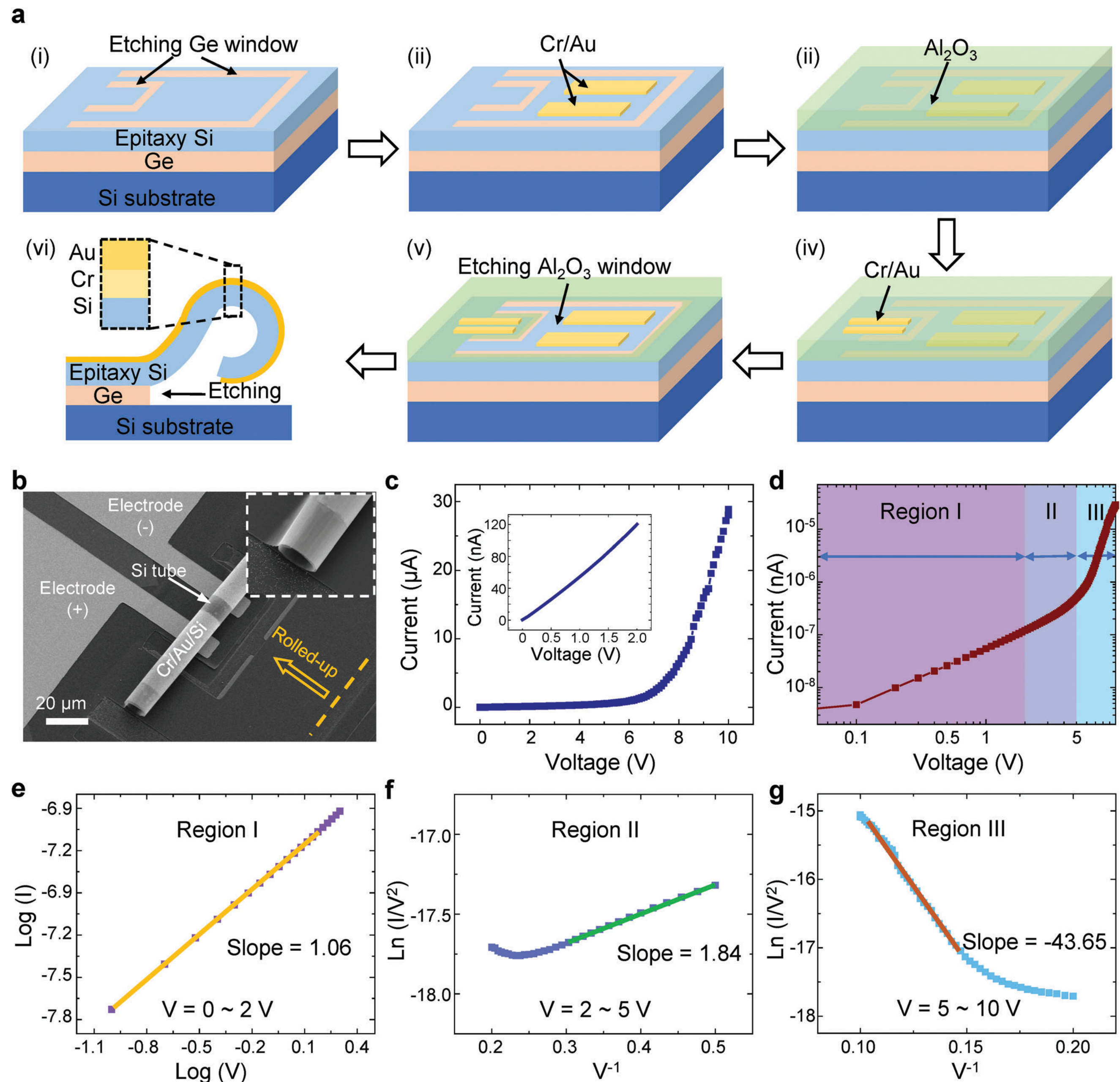

Figure 3. Device fabrication and charge transport mechanism of tubular Si nanomembranes. a) Manufacturing steps for a self-rolled-up 3D tubular Si nanomembrane device. b) SEM image of self-rolled-up Si nanomembrane microtube with electrodes. The rolled-up electrodes are exposed on the outer surface of the microtube in contact with the planar electrodes. The inset shows a side view of a self-rolled-up Si nanomembrane microtube. c) *I–V* curve of Si tube in a linear coordinate. The inset shows linearly correlated current-voltages at 0–1 V. d) *I–V* curve of Si microtube in logarithmic coordinates. Based on the slope of the current curve under different bias voltages, the transport state of the device can be roughly divided into three regions: I (≈0–2 V), II (≈2–5 V), and III (≈5–10 V). e) The charge transport in region I is dominated by Ohmic law. f) The charge transport in region II is dominated by tunneling current. g) The charge transport in region III is dominated by thermally assisted tunneling current.

nanomembranes will be inevitably damaged during the physical or chemical release process. To minimize the damage to the surface of Si nanomembranes, we have designed a special process flow to prepare Si nanomembranes tubular optoelectronic devices, as shown in **Figure 3**a and Figure S12, Supporting Information: i) Defining etching window by photolithography, and etching the epitaxial Si layer by reactive ion etching to expose Ge. ii) Defining electrodes by photolithography and depositing chromium (Cr)/gold (Au) (5 nm/5 nm) with an electron beam evaporation. iii) Depositing 30 nm of Al_2O_3 by ALD. iv) Defining planar electrodes by photolithography and depositing Cr/Au (15 nm/50 nm). v) Using photolithography to define the pattern and etching the exposed Al_2O_3 layer with HF solution to expose the Si nanomembranes and the electrodes deposited in step

 © 2023 Wiley-VCH GmbH

15214095, 2023, 52, Downloaded from https://advanced.onlinelibrary.wiley.com/doi/10.1002/adma.202306715 by Fudan University, Wiley Online Library on [29/01/2026]. See the Terms and Conditions (https://onlinelibrary.wiley.com/terms-and-conditions) on Wiley Online Library for rules of use; OA articles are governed by the applicable Creative Commons License

15214095, 2023, 52, Downloaded from https://advanced.onlinelibrary.wiley.com/doi/10.1002/adma.202306715 by Fudan University, Wiley Online Library on [29/01/2026]. See the Terms and Conditions (https://onlinelibrary.wiley.com/terms-and-conditions) on Wiley Online Library for rules of use; OA articles are governed by the applicable Creative Commons License

(ii). vi) Selectively etching the Ge layer in H_2O_2 solution to release Si nanomembrane with electrodes which rolls up into microtubes. During the subsequent self-rolled-up process, the thinner Cr/Au electrodes deposited on Si nanomembranes are always exposed to the outside of the Si microtubes and form a van der Waals Au–Au contact with the planar electrodes. Once the Si nanomembrane is fully released, the Si wafer will be subsequently immersed in acetone. The microtubes are then isolated from the acetone via a critical point drier, as shown in Figure 3b. Since the Cr/Au electrode deposited by the electron beam evaporation cannot provide sufficient strain comparable to that in epitaxial Si, the diameters of the rolled-up Si microtubes with Cr/Au electrode are ≈11 µm, which exceeds the diameter of the Si microtubes without electrode. Among the prepared microtube devices, we found that the yield of Si microtubes with two turns was higher, and their electrical properties are the most stable during electrical characteristics. Therefore, we selected Si microtubes with two turns as an example for further studying carrier transport behaviors. As shown in Figure 3c, Si microtubes demonstrate linear and nonlinear current-voltage behaviors in the regions of low and high voltages, respectively. When redrawing the current–voltage curve of the device with logarithmic coordinates in Figure 3d, three ranges of different curvatures can be observed, indicating the existence of three transport mechanisms at different bias voltages. At ≈0–2 V, the slope of the ≈Log(I)–Log(V) curve is 1.06 (Figure 3e), indicating that the device is in Ohmic contact and the current was driven by the bias voltage.[47,48] At ≈2–5 V, the slope of the curve $\mathrm{Ln}(I/V^2) \approx V^{-1}$ is 1.84 (Figure 3f). The device was dominated by a tunneling mechanism, and a larger bias voltage could drive electrons through the potential barrier.[49,50] At ≈5–10 V, the slope of the curve $\mathrm{Ln}(I/V^2) \approx V^{-1}$ is −43.65 (Figure 3g), indicating that the device was still dominated by tunneling, but more hot electrons were generated under high bias voltage.[51] Carriers tunneling through the barrier also results in thermal tunneling transport with thermal assistance. This could be caused by the excessive Joule heat generated by the tubular geometry structure under high bias voltage, which cannot be completely dissipated because the tubular Si microtube is suspended on the substrate without large-area contact with substrates, leading to a rapid increase in the temperature of the entire device, further affecting its electrical transmission.

2.4. Photoresponse in VIS-NIRs of Si Microtube Photodetectors

We further investigated tubular photodetectors based on self-rolled-up Si nanomembranes for photodetection in the range of VIS-NIRs. The photocurrent mapping in **Figure 4**a confirms that the light-sensitive region of the Si nanomembrane microtube photodetector is the channel between the preset electrodes, indicating that the electrode layer and Si nanomembrane of our tubular device form a good Ohmic contact, and the device is a photoconductive photodetector. It is an important basis for achieving optical gain to improve photoconductor detection performance. In general, the bandgap of Si is 1.12 eV, and its cutoff wavelength is 1100 nm.[52,53] The typical response peak for bulk Si usually falls within the range of 800–950 nm.[54,55] But for thin Si nanomembranes, the response peak is usually shifted to a range of shorter wavelengths. We should mention that we ignore the radial changes in semiconductor properties of Si microtubes, such as energy band and carrier mobility, as the strain variation introduced by the self-rolling process is trivial in the case of ultrathin nanomembrane. Using a continuously tunable wavelength spectrometer, the spectral response of photodetectors from 400 to 1100 nm was tested, as shown in Figure 4b. The device exhibits a peak response of 700 nm with a response of 330 mA W^{-1}, which is comparable to commercial Si-based photodetector devices. For ultra-thin nanomembrane devices, enhanced performance can be attributed to the tubular geometry that traps incident light and promotes interaction between incident light and Si nanomembranes, thereby improving the light absorption of the device. Performance comparison of the Si tubular photodetectors and previous thin Si-based photodetectors is shown in Table S1, Supporting Information. The dynamic response is measured under 520 nm incident light, and the corresponding photoresponse is shown in Figure S13, Supporting Information. As shown in Figure 4c, the Si tubular photodetector has a fast photoresponse speed with a rise time of 370 µs and a decay time of 440 µs. Dislocations and impurities are generated on the surface of the released Si nanomembranes due to the chemical reaction between the Si nanomembranes and HF/H_2O_2,[56–58] which reduces the response performance and prolongs the response time of the Si tubular photodetectors. In addition, the incident light has two characteristic directions that are respectively parallel and perpendicular to the tube axis for the tubular photodetector, as shown in Figure 4d. In the direction parallel to the microtube axis, the angle-dependent response of the photodetector is fitted by a sinusoidal function, as shown in Figure 4e. This is consistent with conventional planar photoelectric devices. However, in the direction perpendicular to the axis of the microtube, our Si microtube photodetector demonstrates significant angle-independent photodetection. From the perpendicular direction, effective photodetection over ±75° can be achieved, and angle-independent photodetection can be achieved in the range of ±60°, as shown in Figure 4f. We believe that the wide-angle detection characteristics of this tubular photodetector can provide new ideas for inspiring novel approaches in the design of photoelectric imaging systems.

The geometric structure of the tubular Si nanomembrane device can not only enhance the photoresponse but also achieve varying trap effects on linearly polarized light. In the experiment and simulation, the laser was incident vertically from the top of the Si nanomembrane microtubes, and the polarization state of the laser was changed by rotating the half-wave plate or tuning the software setting, respectively. A schematic of the polarized light current test setup is shown in **Figure 5**a. Rotating the half-wave plate alters the polarization angle of the linearly polarized light while maintaining the stable laser power. When the rotation angle of the half-wave plate is $\alpha/2$, the polarization of the linearly polarized light rotates at an angle of α. First, we simulated the electric field distribution of 940 nm polarized light at different polarization angles in the Si nanomembrane microtube structure by using FDTD software, as shown in Figure 5b–h. Accordingly, under the irradiation of 520 nm laser, the simulated electric field distribution is shown in Figure S14, Supporting Information. As the polarization angle α changes from 0° to 90°, the electric vector of linearly polarized light gradually rotates from parallel to perpendicular to the tube axis. The intensity of the electric field in the corresponding microtubes decreases

 © 2023 Wiley-VCH GmbH

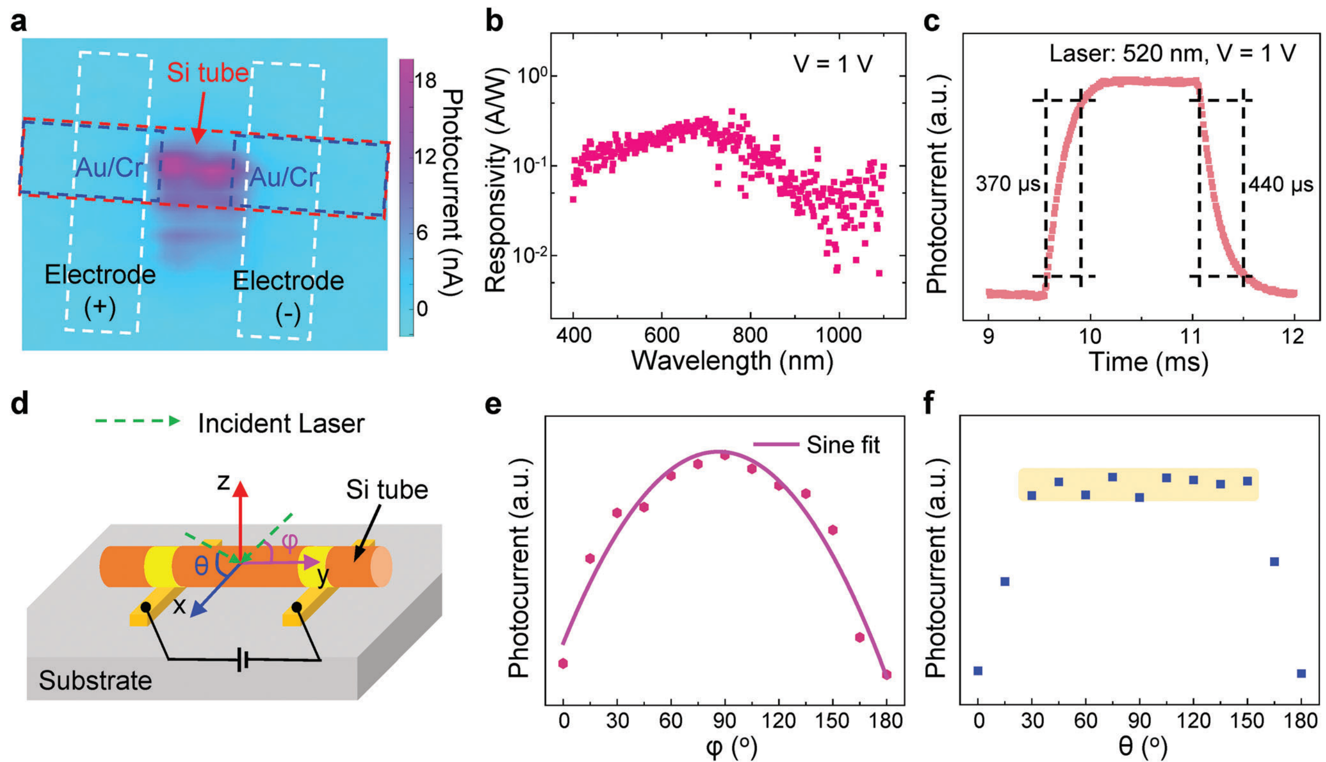

Figure 4. Photoresponse performance of Si microtubule photodetectors. a) The spatial photocurrent map obtained by laser scanning (wavelength 520 nm, power 15 µW, spot size 1 µm) over the sample with 1 V bias voltage. The photocurrent occurs exactly at the bare Si microtube, which is marked by a blue dashed line. b) Photoresponsivity of the Si microtube photodetector for incident light wavelengths ranging from 400 to 1100 nm at V = 1 V. c) 90–10% rise and decay time of photocurrent are measured as 370 and 440 µs, respectively. d) Schematic diagram of the setup of angle-dependent photocurrent test. The bright green arrow represents the direction of the incident laser. In *xyz* coordinates, the coordinate origin is at the symmetrical center point of the Si microtube, the *x*-axis (*y*-axis) is perpendicular (parallel) to the tube axis, and the *z*-axis is perpendicular to the substrate. In the *xz* (*yz*) plane, the laser is incident at an angle of θ (φ) to the *x*-axis (*y*-axis). e) The photocurrent curve is dependent on the laser incident angle φ and fitted with the sin function. f) The photocurrent curve as a function of the laser incident angle θ. The responsivity in 30° to 150° highlighted in yellow has no angle dependence.

significantly, indicating that the coupling effect of tubular structures on linearly polarized light in different directions varies. Limitation of the polarized light at varying angles presents an advantage for the detection of polarization in Si nanomembrane devices. The observed polarization anisotropy is well explained by classical electromagnetic theory (Note S1, Supporting Information). Significant polarization sensitivity is attributed to the substantial dielectric contrast between the microtube wall and its surrounding air environment. We quantitatively simulate this effect by treating Si microtubes as infinite dielectric ring cylinders in a vacuum. When the incident field is parallel to the axial polarization of the microtube, the electric field inside the ring cylinder is enhanced compared with the polarization that is perpendicular to the microtube axis. To investigate this quantitatively, the photocurrent at the most sensitive polarization angle is divided by the photocurrent at the least sensitive polarization angle to get dichroic ratios. Figures 5i,j,k show that the dichroic ratios of the device for 940, 830, and 520 nm laser polarization detection are 1.24, 1.16, and 1.14, respectively, which are comparable to those of most non-lens-assisted polarization photodetectors. More, we compared the performance of polarization detection photodetectors realized by the geometrical structure in recent years. Our Si microtubular photodetectors have good performance in response rate and response time (Figure S15, Supporting Information).

3. Conclusion

In summary, we obtained high-quality, freestanding single-crystalline Si nanomembranes by wet etching the Ge sacrificial layer. The release of residual strain introduced by lattice mismatch at the Si-Ge epitaxial interface drives Si nanomembranes to self-assemble into microtube structures. The thickness-dependent self-rolled-up microtube radius and strain distribution of nanomembranes were analyzed experimentally and theoretically. Despite the release process, the self-rolled-up Si nanomembrane still maintains good electrical conduction characteristics and sensitive VIS-NIRs detection performance, especially in the fields of wide-angle optical coupling detection and polarization-sensitive detection. In addition, our self-rolled-up epitaxial single-crystalline nanomembrane microtube strategy demonstrates the potential to establish novel avenues to produce Si, Ge, and other materials-based advanced electronic and optoelectronic devices, aiming at achieving next-generation optoelectronic integrated chips featuring novel functionalities.

© 2023 Wiley-VCH GmbH

15214095, 2023, 52, Downloaded from https://advanced.onlinelibrary.wiley.com/doi/10.1002/adma.202306715 by Fudan University, Wiley Online Library on [29/01/2026]. See the Terms and Conditions (https://onlinelibrary.wiley.com/terms-and-conditions) on Wiley Online Library for rules of use; OA articles are governed by the applicable Creative Commons License

15214095, 2023, 52, Downloaded from https://advanced.onlinelibrary.wiley.com/doi/10.1002/adma.202306715 by Fudan University, Wiley Online Library on [29/01/2026]. See the Terms and Conditions (https://onlinelibrary.wiley.com/terms-and-conditions) on Wiley Online Library for rules of use; OA articles are governed by the applicable Creative Commons License

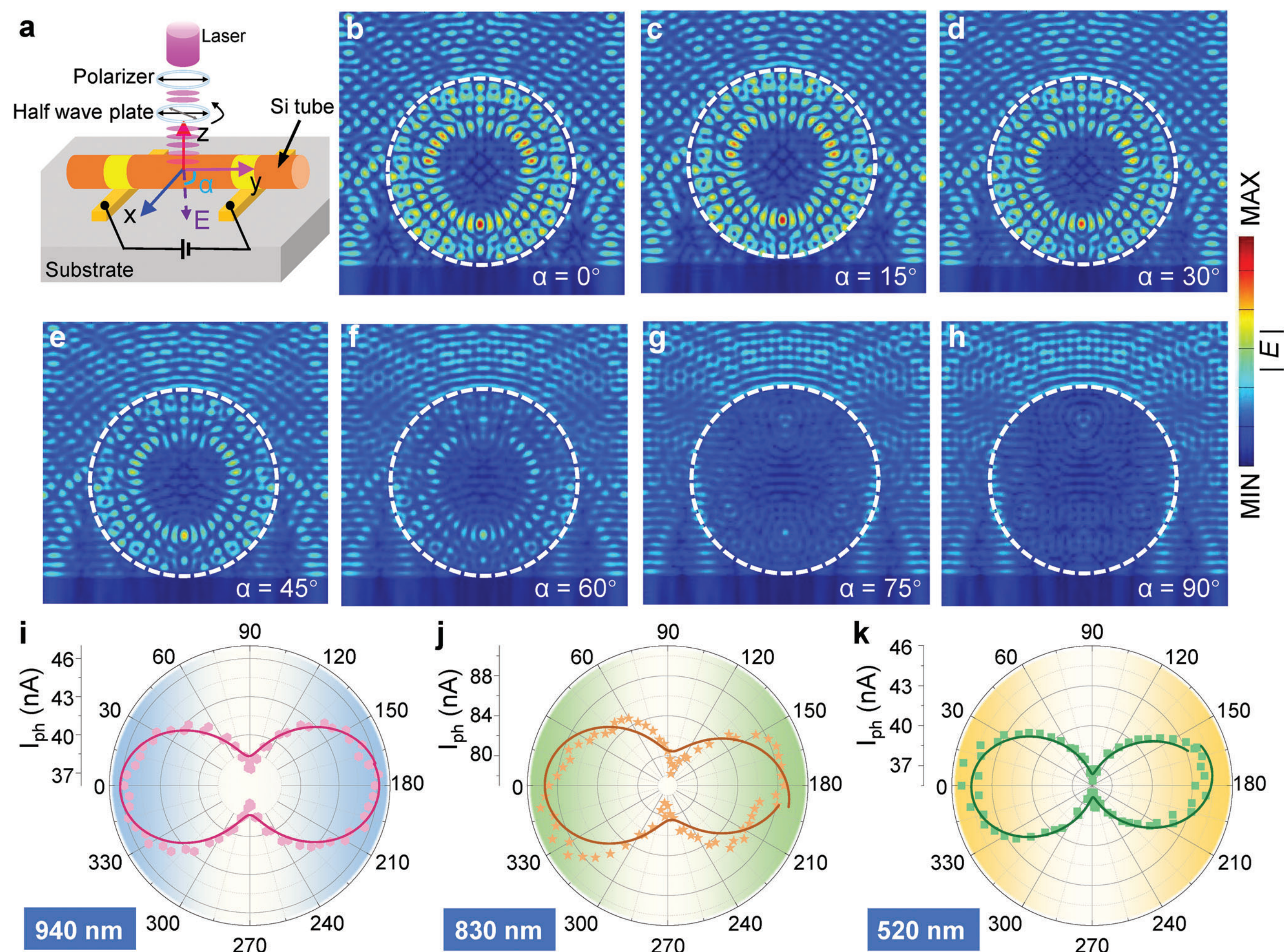

Figure 5. Polarization detection characteristics of self-rolled-up Si microtubular photodetector. a) Schematic of polarization detection test setup. The incident laser is modulated by a polarizer and a half-wave plate and irradiates perpendicularly to the device. The *y*-axis is oriented parallel to the tube axis, while the *x*-axis is perpendicular to it. The angle between the direction of the electric vector of linearly polarized light and the *y*-axis is defined as α. b–h) Simulated electric field distribution in Si microtube illuminated by linearly polarized light (940 nm) for $\alpha = 0°–90°$ with a step of 15°. The purple circles represent the cross-section of self-rolled-up Si nanomembranes. Measured photocurrents as a function of polarizer angle α under linearly polarized illuminations at 940 (i), 830 (j), and 520 nm (k) from self-rolled-up Si microtube photodetector.

4. Experimental Section

Fabrication of Si Microtubes: First, the 40 nm Ge layer was epitaxially grown on a Si wafer, and then Si layers with thicknesses of 6, 10, 20, or 30 nm were epitaxially grown on Ge. The instrument used was solid-source MBE and the growth temperature was 280 °C. The concentration of phosphorus dopant in epitaxial Si was ≈4×10^{17} cm^{-3}. The epitaxial Si was initially cleaned using hydrofluoric acid (HF) acid to remove the native oxide layer from the surface. A layer of photoresist with about 2 µm thickness was spin-coated and etching windows were defined by photolithography. After development, the window was exposed and etched by reactive ion etching for 40 s (35 sccm SF_6 and 18 sccm CHF_3 flow, 30 mTorr chamber pressure, and 50 W etching power). The photoresist layer was then removed by ultrasonication in acetone for 120 s. Cr/Au electrodes with different thicknesses were deposited by e-beam evaporation. In the microtube fabrication process with electrodes, 30 nm Al_2O_3 was deposited with ALD to isolate electrical conduction between the planar metal electrode and the substrate. For the rolling process, patterned Si nanomembranes with/without electrodes were released from the substrate by using 30% H_2O_2 solution at 70 °C for 15 min. Finally, a critical point dryer (CPD) was applied to dry the self-rolled-up Si microtubes, avoiding structural collapse.

Materials and Structure Characterization of Si Nanomembranes: A Lab Ram HR800 from HORIBA spectrometer and an Olympus ×100 objective lens were used for Raman measurements. The structure of self-rolled-up Si nanomembranes was characterized via SEM. Before the characterization by TEM, the sample lamella was cut by FIB, and the deposition of the Pt layer was used to protect the surface of the Si nanomembrane during the preparation process. TEM and STEM images were collected on JEOL JEM-ARM200F at 200 kV.

Electrical and Optoelectronic Characterization of Si Microtubes: The electrical properties of Si nanomembranes were performed on a Keysight B2902B. The VIS-NIRs photoresponse measurement was under Xenon lamps with a spot diameter of ≈100 µm to ensure uniform power on the device. All other optoelectronic measurements were taken by an MStarter 200 optoelectronic measurement system from Maita Optoelectronic Technology Co., LTD.

Optical Simulation: Simulation of electrical field distribution in microtube Si nanomembranes was realized by commercial software Lumerical FDTD solutions. The model consisted of a Si tubular structure (outer

 © 2023 Wiley-VCH GmbH

15214095, 2023, 52, Downloaded from https://advanced.onlinelibrary.wiley.com/doi/10.1002/adma.202306715 by Fudan University, Wiley Online Library on [29/01/2026]. See the Terms and Conditions (https://onlinelibrary.wiley.com/terms-and-conditions) on Wiley Online Library for rules of use; OA articles are governed by the applicable Creative Commons License

diameter D_{outer} = 10 µm, inner diameter D_{inner} = 9.94 µm, length L = 40 µm) on epitaxy-Si/Ge/Si sandwich structure ($t_{epitaxy\text{-}Si}$ = 30 nm, t_{Ge} = 40 nm, $t_{substrate\text{-}Si}$ = 100 µm, L = 40 µm) to simulate the tubular Si nanomembrane on the substrate. The boundary condition of the direction perpendicular to the substrate was set to a perfect match layer, while the periodical boundary condition was applied in the direction parallel to the substrate due to the periodicity of the Si microtube array. A plane wave (λ = 940 nm and 520 mm, spot radius r = 1 mm) was utilized to simulate an incident-polarized light source.

Supporting Information

Supporting Information is available from the Wiley Online Library or from the author.

Acknowledgements

This work was supported by the National Key Technologies R&D Program of China (2021YFE0191800 and 2021YFA0715302), the National Natural Science Foundation of China (61975035), and the Science and Technology Commission of Shanghai Municipality (21142200200, 22ZR1405000, 21YF1401600, and 21ZR1403500). Part of the sample fabrication was performed at the Fudan Nano-fabrication Laboratory.

Conflict of Interest

The authors declare no conflict of interest.

Author Contributions

B.W. and Z.Zhang contributed equally to this work. Y.M. conceived the idea for the project and designed the experiments. B.W., C.Y., and Z.Zhang fabricated the devices and performed the electronic and optoelectronic measurements. Z.Zhang, T.C., and Y.W. performed optical simulations and calculations. B.W., Z.Zheng, and X.L. performed the STEM experiments and analyzed the data. J.W., H.L., and B.W. performed the Raman experiments. B.W., G.H., and Y.M. co-wrote the manuscript. All authors discussed the results and commented on the manuscript.

Data Availability Statement

The data that support the findings of this study are available from the corresponding author upon reasonable request.

Keywords

photodetectors, polarization-sensitivity, self-rolled-up microtubes, single-crystalline Si nanomembranes

Received: July 9, 2023
Revised: September 9, 2023
Published online: November 20, 2023

[1] H. Wang, H. Zhen, S. Li, Y. Jing, G. Huang, Y. Mei, W. Lu, *Sci. Adv.* **2016**, *2*, e1600027.
[2] M. M. Roberts, L. J. Klein, D. E. Savage, K. A. Slinker, M. Friesen, G. Celler, M. A. Eriksson, M. G. Lagally, *Nat. Mater.* **2006**, *5*, 388.
[3] D. Ji, S. Cai, T. R. Paudel, H. Sun, C. Zhang, L.u Han, Y. Wei, Y. Zang, M. Gu, Y.i Zhang, W. Gao, H. Huyan, W. Guo, D. Wu, Z. Gu, E. Y. Tsymbal, P. Wang, Y. Nie, X. Pan, *Nature* **2019**, *570*, 87.
[4] Y. Meng, J. Feng, S. Han, Z. Xu, W. Mao, T. Zhang, J. Kim, I. Roh, Y. Zhao, D. Kim, Y. Yang, J. Lee, L. Yang, C. Qiu, S. Bae, *Nat. Rev. Mater.* **2023**, *8*, 498.
[5] J. A. Rogers, M. G. Lagally, R. G. Nuzzo, *Nature* **2011**, *477*, 45.
[6] D. Karnaushenko, T. Kang, V. K. Bandari, F. Zhu, O. G. Schmidt, *Adv. Mater.* **2020**, *32*, 1902994.
[7] X. Cheng, Y. Zhang, *Adv. Mater.* **2019**, *31*, 1901895.
[8] G. Huang, Y. Mei, *Small* **2018**, *14*, e1703665.
[9] B. Zhao, Z. Wan, Y. Liu, J. Xu, X. Yang, D. Shen, Z. Zhang, C. Guo, Q.i Qian, J. Li, R. Wu, Z. Lin, X. Yan, B. Li, Z. Zhang, H. Ma, B.o Li, X. Chen, Y.i Qiao, I. Shakir, Z. Almutairi, F. Wei, Y. Zhang, X. Pan, Y.u Huang, Y. Ping, X. Duan, X. Duan, *Nature* **2021**, *591*, 385.
[10] B. Wu, Z. Zhang, C. Wang, E. Song, J. Cui, G. Huang, P. Zhou, Z. Di, Y. Mei, *Appl. Phys. Lett.* **2022**, *121*, 060503.
[11] Y. Guo, B. Peng, R. Qiu, G. Dong, Y. Yao, Y. Zhao, Z. Zhou, M. Liu, *Adv. Funct. Mater.* **2023**, *33*, 2213668.
[12] G. Dong, S. Li, M. Yao, Z. Zhou, Y.-Q. Zhang, X. Han, Z. Luo, J. Yao, B. Peng, Z. Hu, H. Huang, T. Jia, J. Li, W. Ren, Z.-G. Ye, X. Ding, J. Sun, C.-W. Nan, L.-Q. Chen, J. Li, M. Liu, *Science* **2019**, *366*, 475.
[13] D. Lu, D. J. Baek, S. S. Hong, L. F. Kourkoutis, Y. Hikita, H. Y. Hwang, *Nat. Mater.* **2016**, *15*, 1255.
[14] C. Müller, I. Neckel, M. Monecke, V. Dzhagan, G. Salvan, S. Schulze, S. Baunack, T. Gemming, S. Oswald, V. Engemaier, D. H. Mosca, *RSC Adv.* **2016**, *6*, 72568.
[15] C.-Z. Ning, L. Dou, P. Yang, *Nat. Rev. Mater.* **2017**, *2*, 17070.
[16] W. Chen, Y. Wu, Y. Yue, J. Liu, W. Zhang, X. Yang, H. Chen, E. Bi, I. Ashraful, M. Grätzel, L. Han, *Science* **2015**, *350*, 944.
[17] Z. Zhu, C. Zhu, L. Yang, Q. Chen, L. Zhang, J. Dai, J. Cao, S. Zeng, Z. Wang, Z. Wang, W. Zhang, J. Bao, L. Yang, Y. Yang, B.o Chen, C. Yin, H. Chen, Y. Cao, H. Gu, J. Yan, N. Wang, G. Xing, H. Li, X. Wang, S. Li, Z. Liu, H. Zhang, L. Wang, X. Huang, W. Huang, *Nat. Mater.* **2022**, *21*, 1042.
[18] J. Liu, X. Sun, D. Pan, X. Wang, L. C. Kimerling, T. L. Koch, J. Michel, *Opt. Express* **2007**, *15*, 11272.
[19] J. Liu, X. Sun, L. Kimerling, J. Michel, *Opt. Express* **2009**, *34*, 1738.
[20] X. Sun, J. Liu, L. Kimerling, J. Michel, *Opt. Express* **2009**, *34*, 1198.
[21] X. Li, Z. Yin, X. Zhang, Y.e Wang, D. Wang, M. Gao, J. Meng, J. Wu, J. You, *Adv. Mater. Technol.* **2019**, *4*, 1800695.
[22] S. Shrestha, M. Coile, M. Zhu, M. Souri, J. Kim, R. Pandey, J. W. Brill, J. Hwang, J.-W. Kim, A. Seo, *ACS Appl. Nano Mater.* **2020**, *3*, 6310.
[23] W. S. Wong, T. Sands, N. W. Cheung, *Appl. Phys. Lett.* **1998**, *72*, 599.
[24] S. Xu, Z. Yan, K.-I. Jang, W. Huang, H. Fu, J. Kim, Z. Wei, M. Flavin, J. Mccracken, R. Wang, A. Badea, Y. Liu, D. Xiao, G. Zhou, J. Lee, H. U. Chung, H. Cheng, W. Ren, A. Banks, X. Li, U. Paik, R. G. Nuzzo, Y. Huang, Y. Zhang, J. A. Rogers, *Science* **2015**, *347*, 154.
[25] T. Deng, Z. Zhang, Y. Liu, Y. Wang, F. Su, S. Li, Y. Zhang, H. Li, H. Chen, Z. Zhao, Y. Li, Z. Liu, *Nano Lett.* **2019**, *19*, 1494.
[26] X. Hou, R. Pan, Q. Yu, K. Zhang, G. Huang, Y. Mei, D. W. Zhang, P. Zhou, *Small* **2019**, *15*, e1803876.
[27] Z. Tian, B. Xu, B.o Hsu, L. Stan, Z. Yang, Y. Mei, *Nano Lett.* **2018**, *18*, 3017.
[28] A. K. Katiyar, K. Y. Thai, W. S. Yun, J. Lee, J.-H. Ahn, *Sci. Adv.* **2022**, *6*, eabb0576.
[29] S. Yang, Y. Wang, Y.e Kong, G. Huang, Z. Zhao, Y. Wang, B. Xu, J. Cui, Y. Mei, *Adv. Opt. Mater.* **2021**, *10*, 2102158.
[30] D. Shahrjerdi, B. Hekmatshoar, S. W. Bedell, M. Hopstaken, D. K. Sadana, *J. Electron. Mater.* **2011**, *41*, 494.
[31] F. Wen, E. Tutuc, *Nano Lett.* **2018**, *18*, 94.
[32] E. Mohapatra, D. Jena, S. Das, C.k Maiti, T. P. Dash, *Phys. Scr.* **2023**, *98*, 065919.

© 2023 Wiley-VCH GmbH

[33] J. M. Baribeau, T. E. Jackman, P. Maigné, D. C. Houghton, M. W. Denhoff, *J. Vac. Sci. Technol., A* **1987**, *5*, 1898.
[34] H. Ye, J. Yu, *Sci. Technol. Adv. Mater.* **2014**, *15*, 024601.
[35] A. Heintz, B. Ilahi, A. Pofelski, G. Botton, G. Patriarche, A. Barzaghi, S. Fafard, R. Arès, G. Isella, A. Boucherif, *Nat. Commun.* **2022**, *13*, 6624.
[36] Q. Guo, Z. Di, M. G. Lagally, Y. Mei, *Mater. Sci. Eng.: R: Rep.* **2018**, *128*, 1.
[37] V. B. Shenoy, D. H. Gracias, *MRS Bull.* **2012**, *37*, 847.
[38] Z. Jiang, W. Zhang, L. Yan, X. Niu, *Mater. Sci. Eng., B* **2005**, *119*, 182.
[39] H. P. Sun, Y. B. Chen, X. Q. Pan, D. Z. Chi, R. Nath, Y. L. Foo, *Appl. Phys. Lett.* **2005**, *86*, 071904.
[40] B. Xu, X. Zhang, Z. Tian, D.i Han, X. Fan, Y. Chen, Z. Di, T. Qiu, Y. Mei, *Nat. Commun.* **2019**, *10*, 5019.
[41] Z. Tian, S. Li, S. Kiravittaya, B. Xu, S. Tang, H. Zhen, W. Lu, Y. Mei, *Nano Lett.* **2018**, *18*, 8035.
[42] C. Xu, X. Wu, G. Huang, Y. Mei, *Adv. Mater. Technol.* **2019**, *4*, 1800486.
[43] M. Huang, H. Yan, C. Chen, D. Song, T. F. Heinz, J. Hone, *Proc. Natl. Acad. Sci. U. S. A.* **2009**, *106*, 7304.
[44] J.-U. Lee, S. Woo, J. Park, H. C. Park, Y.-W. Son, H. Cheong, *Nat. Commun.* **2017**, *8*, 1370.
[45] G. P. Nikishkov, *J. Appl. Phys.* **2003**, *94*, 5333.
[46] E. Song, Z. Guo, G. Li, F. Liao, G. Li, H. Du, O. G. Schmidt, M. Kim, Y. Yi, W. Bao, Y. Mei, *Adv. Electron. Mater.* **2019**, *5*, 1900232.
[47] V. D. Mihailetchi, J. Wildeman, P. W. M. Blom, *Phys. Rev. Lett.* **2005**, *94*, 126602.
[48] Q. Liu, W. Guan, S. Long, R. Jia, M. Liu, J. Chen, *Appl. Phys. Lett.* **2008**, *92*, 012117.
[49] J.-G. Park, W.-S. Nam, S.-H.o Seo, Y.-G. Kim, Y.-H. Oh, G.-S. Lee, U.-G. Paik, *Nano Lett.* **2009**, *9*, 1713.
[50] Y.-E. Syu, T.-C. Chang, T.-M. Tsai, G.-W. Chang, K.-C. Chang, J.-H. Lou, Y.a-H. Tai, M.-J. Tsai, Y.-L. Wang, S. M. Sze, *IEEE Electron Device Lett.* **2012**, *33*, 342.
[51] H. Sun, Q.i Liu, S. Long, H. Lv, W. Banerjee, M. Liu, *J. Appl. Phys.* **2014**, *116*, 154509.
[52] Z. Huang, J. E. Carey, M. Liu, X. Guo, E. Mazur, J. C. Campbell, *Appl. Phys. Lett.* **2006**, *89*, 033506.
[53] M. K. Emsley, O. Dosunmu, M. S. Unlu, *IEEE Photonics Technol. Lett.* **2002**, *14*, 519.
[54] H. Xu, Y. Yang, J. Tan, L. Chen, H. Zhu, Q. Sun, *IEEE Electron Device Lett.* **2022**, *43*, 1077.
[55] M. Casalino, G. Coppola, M. Iodice, I. Rendina, L. Sirleto, *Sensors* **2010**, *10*, 10571.
[56] S. W. Park, H. Kim, E. Chagarov, S. Siddiqui, B. Sahu, N. Yoshida, J. Kachian, R. Feenstra, A. C. Kummel, *Surf. Sci.* **2016**, *652*, 322.
[57] R. C. Newman, *Rep. Prog. Phys.* **1982**, *45*, 1163.
[58] X. D. Pi, L. Mangolini, S. A. Campbell, U. Kortshagen, *Phys. Rev. B* **2007**, *75*, 085423.

© 2023 Wiley-VCH GmbH

15214095, 2023, 52, Downloaded from https://advanced.onlinelibrary.wiley.com/doi/10.1002/adma.202306715 by Fudan University, Wiley Online Library on [29/01/2026]. See the Terms and Conditions (https://onlinelibrary.wiley.com/terms-and-conditions) on Wiley Online Library for rules of use; OA articles are governed by the applicable Creative Commons License